



Qualitative measurement of spatial shielding isotopics via Compton imaging neutron-induced gamma rays using 3-D CdZnTe detectors

David Goodman^{*}, Jiawei Xia, Zhong He

Nuclear Engineering & Radiological Sciences, 2355 Bonisteel Blvd., 1906 Cooley Bldg., Ann Arbor, MI 48109-2104, United States

ARTICLE INFO

Keywords:

3-D CdZnTe
Compton imaging
Shielding characterization
Neutron-induced gamma rays

ABSTRACT

Characterization of shielding around special nuclear materials (SNMs) in unknown objects is important for homeland security, international safeguards and potential nuclear disarmament verification. Shielding modulates source photons and neutrons, complicating radiation-based SNM characterization, and indicates object purpose and guides response. Previous gamma-ray-based shielding detection algorithms only estimate effective shielding atomic number and areal thickness, complicating the characterization of compound shields comprised of multiple elements. Neutron-induced gamma rays, from inelastic scatter or capture, provide a complementary, isotope-specific shielding signal which can be localized using Compton imaging. Qualitative, angularly-resolved isotopic distributions in a compound shield were measured using polyethylene and polyvinyl chloride targets, excited via a single PuBe neutron source, and a 3-D, position-sensitive CdZnTe imaging spectrometer. Hydrogen capture gamma rays, which predominately originate from the polyethylene target, were well separated in angular space from chlorine capture gamma rays, originating in the polyvinyl chloride target, using Compton imaging. The described qualitative probe of spatial shielding isotopics can be immediately applied on any commercial gamma-ray imaging spectrometer without modification.

1. Introduction

In nuclear emergency response, objects that contain special nuclear materials (SNMs) must be characterized as quickly and thoroughly as possible. Unknown shielding can complicate the characterization of special nuclear materials by modulating emitted source neutron and photon signals. For example, without detailed characterization of shielding, uranium and plutonium grading measurements can be biased [1–3]. Furthermore, shielding around SNM must be characterized as it indicates how the material is used. For example, shielding around SNMs must be characterized in nuclear disarmament treaties as weapon dismantlement, commonly defined as the separation of high explosives and SNMs, can be confirmed by the presence, or lack thereof, low-Z shielding [4,5].

Shielded objects can be characterized using either passive or active techniques. Active measurements use high-energy photon or neutron sources to interrogate objects, exciting neutron and gamma-ray signals inside the source and shielding [6]. Contrastingly, passive measurements only leverage neutron and photon signals that are naturally emitted from the source [7]. Active measurement typically produces larger, more-detectable radiation signals, but is more intrusive than passive measurement which limits its use. Luckily plutonium, a commonly encountered SNM, is both a strong gamma ray and fast neutron emitter that can be measured passively [7]. However neutron signals

leaving an object are ambiguously perturbed by shielding, revealing little about shielding composition. Therefore this work focuses on leveraging passively emitted gamma-ray signals from bright sources, such as plutonium, to characterize shielding in unknown objects.

Previous gamma-ray based shielding identification algorithms measure the spectral perturbation of gamma rays leaking out of an object to characterize shielding around SNM [8,9]. These algorithms can be applied on directional gamma-ray spectra from coded aperture or Compton imaging to estimate directional shielding [10,11]. However, gamma-ray-based shielding detection algorithms can only estimate shielding areal thickness and effective atomic number, not the presence of individual elements, in compound shields such as plastics or explosives. This limits algorithm use as realistic geometries often contain compound shields.

In combined neutron and gamma-ray fields, such as those around plutonium, characteristic neutron-induced gamma rays from neutron interactions in shielding offer a complimentary, isotope-specific signal of shielding composition [12,13]. Gamma rays from inelastic scatter and neutron capture can be Compton imaged to provide spatially-resolved estimates of shielding isotopics around SNMs.

We demonstrate the novel detection and spatially resolved characterization of shielding isotopics in polyethylene and polyvinyl chloride plastic targets, simultaneously excited by a single fast neutron source,

^{*} Corresponding author.

E-mail address: dgoodma@umich.edu (D. Goodman).

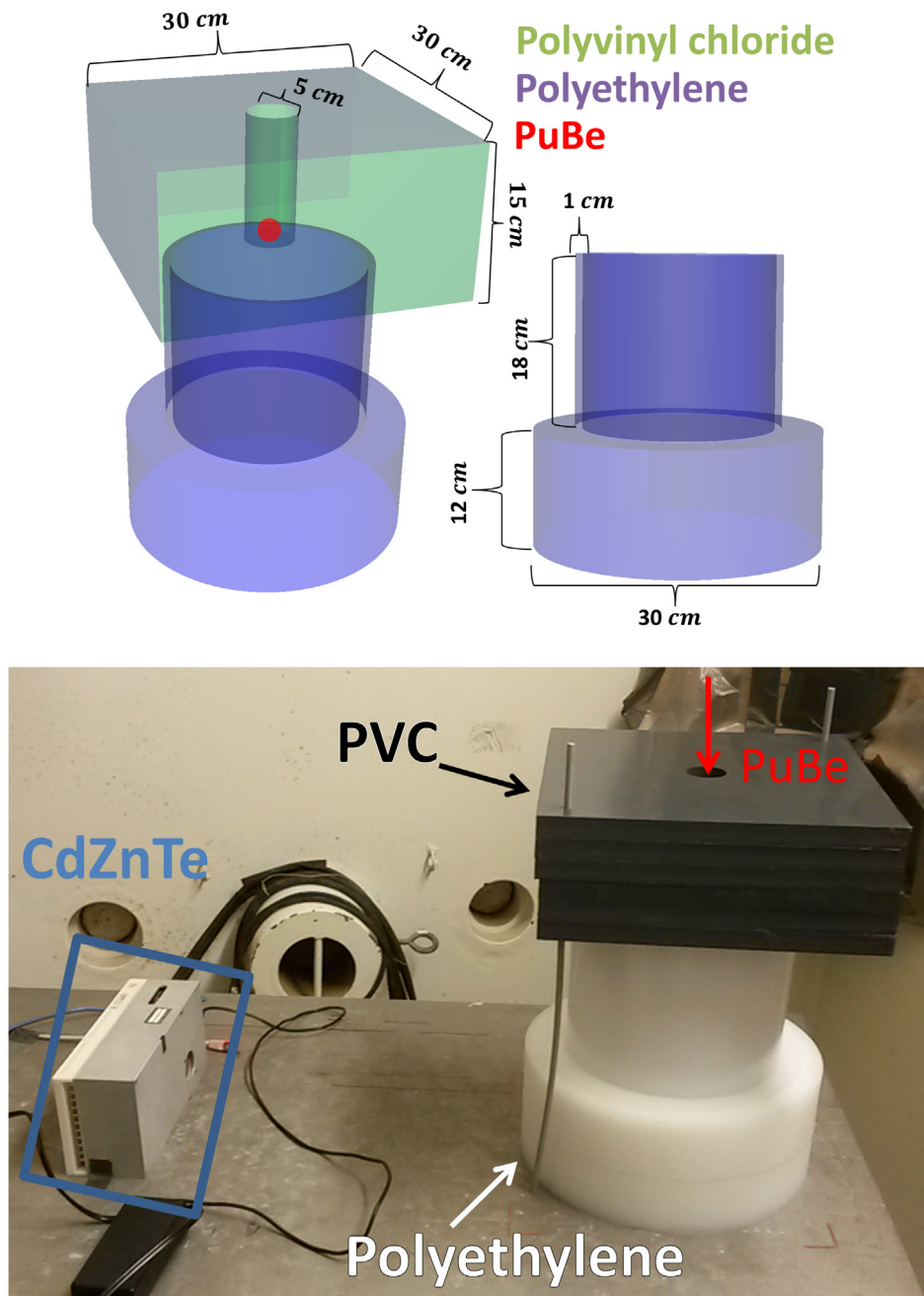


Fig. 1. (Top) MCNP rendering of the dumbbell geometry consisting of two, large PVC and PE targets separated by a low-mass spacer. Note the 18 cm PE spacer was hollow to minimize neutron interactions between the targets. (Bottom) Measurement setup before elevating the detector towards the center of the dumbbell. The detector was eventually elevated 15 cm above the table surface, 45 cm away from the target centerline.

using an array of pixelated CdZnTe detectors and Compton imaging. Difficulties in Compton imaging high-energy gamma rays are discussed. The demonstrated technique can be combined with any traditional gamma-ray shielding detection algorithm and easily implemented on commercial, off-the-shelf, gamma-ray imaging spectrometers [14,15].

2. Background

2.1. Neutron capture and inelastic scatter

Fission and (α, n) neutrons are typically born with mean energies exceeding one MeV. These fast, energetic neutrons interact with atomic nuclei, depositing energy, until reaching thermal energies of roughly 0.025 eV. During this thermalization process, neutrons with sufficient

energy can inelastically scatter off a nucleus, exciting the nucleus to energetic levels above the ground state. The now excited nucleus deexcites to the ground state via emission of one or more gamma rays with energies corresponding to the energy differences between nuclear levels. Energy levels of each nuclei are unique, therefore characteristic gamma rays from inelastic scatter unambiguously signal the presence of certain isotopes.

Neutrons can be permanently absorbed by a nucleus through neutron capture. Neutron capture cross sections typically increase with decreasing neutron energy. However some nuclei, such as ^{35}Cl , have strong capture resonances at higher energies. Neutron capture often leaves the resulting nucleus in an excited state, which deexcites to ground via emitting one or more characteristic gamma rays with energies corresponding to differences in nuclear energy levels. Similarly, the

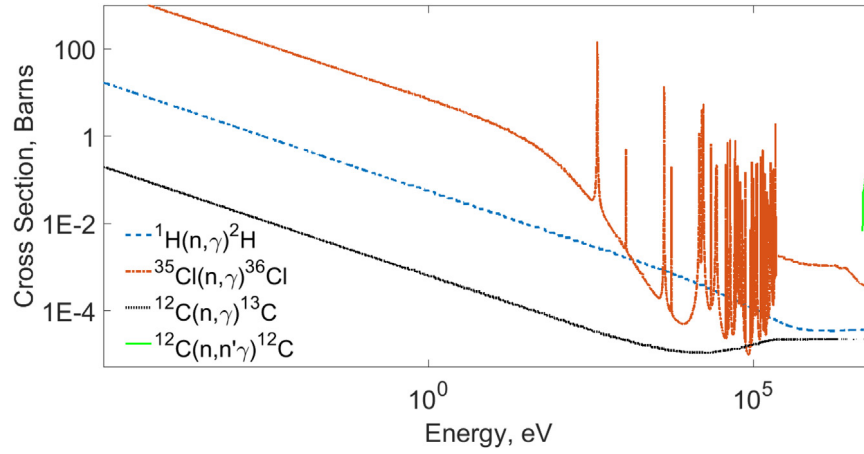


Fig. 2. Neutron inelastic scatter and capture cross sections as a function of energy for ^{35}Cl , ^1H and ^{12}C . Note the resonant capture behavior in ^{35}Cl and threshold energy for inelastic scatter on ^{12}C . Note that the thermal capture cross section of ^{35}Cl is much larger than ^1H which is much larger than ^{12}C .

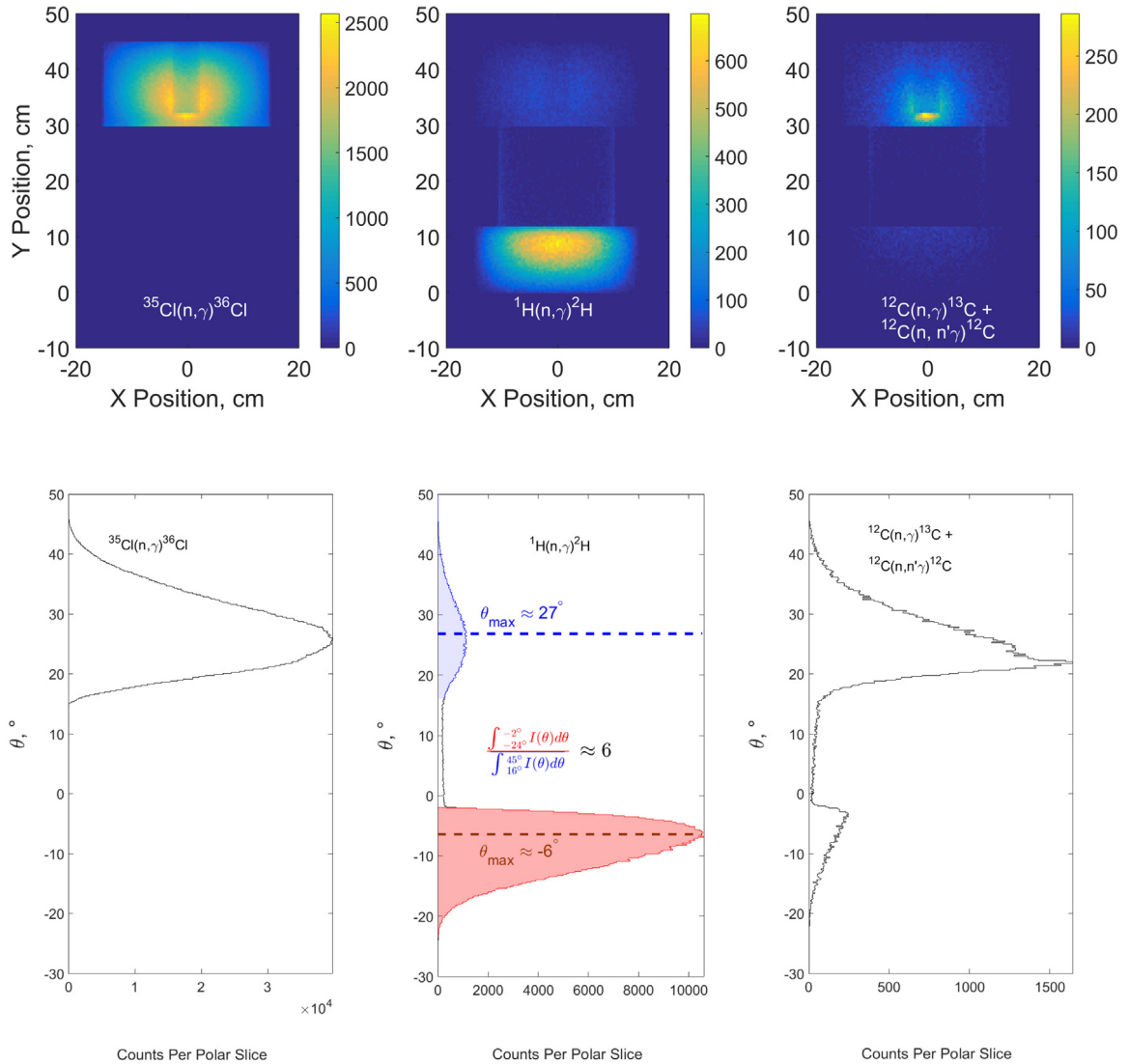


Fig. 3. (Top) Cartesian projection of simulated ^{35}Cl , ^1H and ^{12}C neutron inelastic scatter and capture in the dumbbell geometry. The PVC and PE targets span $y = [30, 45]$ cm and $y = [0, 15]$ cm respectively. (Bottom) Interaction locations on the Cartesian grid are converted to spherical coordinates using $\vec{r} = [0, 15, 45]$ cm as an origin. Polar slices, computed by summing across the azimuthal direction, show clear separation between capture regions.

unique energies of neutron capture gamma rays unambiguously signal the presence of certain isotopes.

The spatial distribution of neutron inelastic scatter and capture interactions in an object is strongly coupled to the free neutron density.

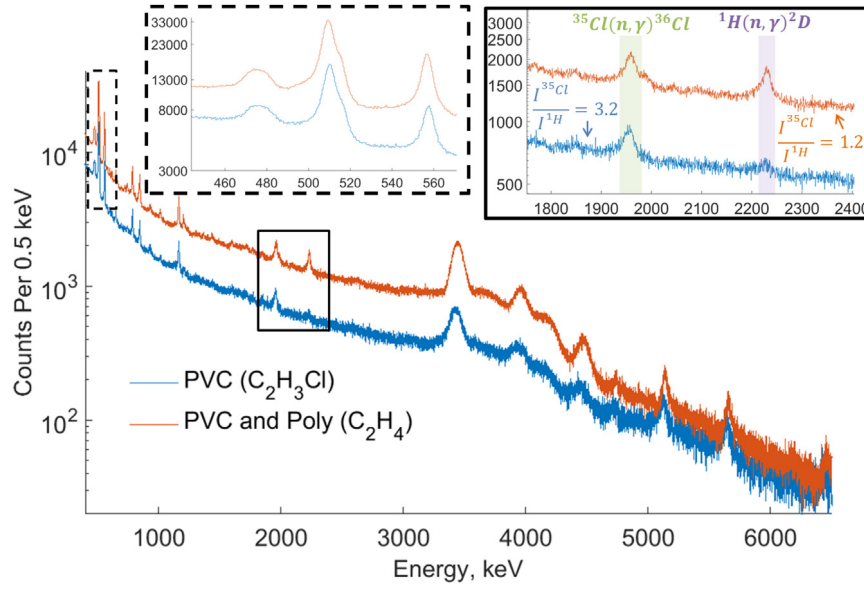


Fig. 4. Gamma-ray spectra from the PVC target alone (blue) and the dumbbell geometry with PVC and PE (orange). The ratio of ^1H to ^{35}Cl capture increases with the addition of PE as shown in the solid, inset panel. Contamination the 517 keV ^{35}Cl capture gamma ray by pair production is seen in the dashed, inset panel. (For interpretation of the references to color in this figure legend, the reader is referred to the web version of this article.)

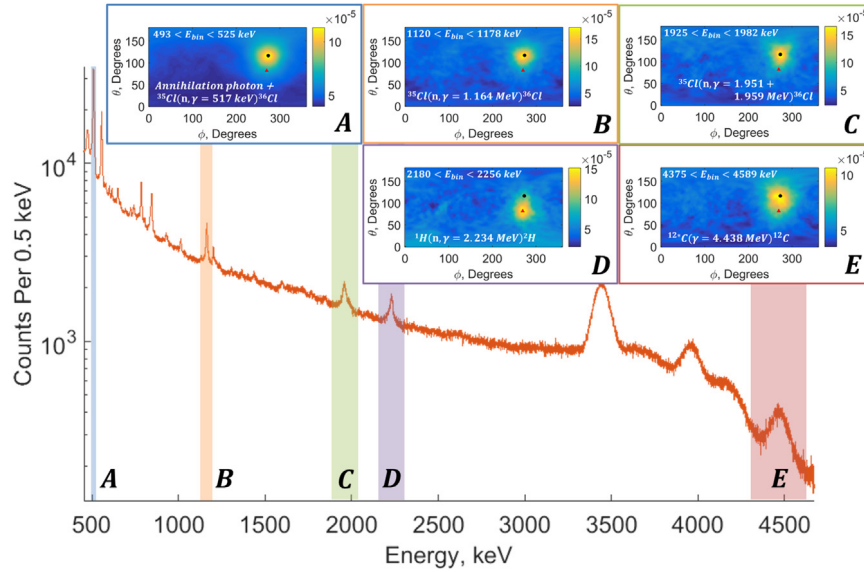


Fig. 5. Compton simple back-projection of $^{35}\text{Cl}(n,\gamma)^{36}\text{Cl}$, $^1\text{H}(n,\gamma)^2\text{H}$ and $^{12}\text{C}(n,\gamma)^{13}\text{C}$ gamma-ray lines. Compton back-projections of individual energy bins are color coded and lettered. A red triangle and black circle are placed in the center of hydrogen and chlorine hotspots respectively to guide the eyes.

Given some neutron source, the reaction rate of interaction type i in spatial region $d\vec{r}$ about \vec{r} of an object is

$$I_i(\vec{r}) = \int_0^{E_{\max}} v(E) N(\vec{r}, E) \Sigma_i(\vec{r}, E) dE \quad (1)$$

where $N(\vec{r}, E)$ is the free neutron density in $d\vec{r}$ about \vec{r} and dE about E , $v(E)$ is neutron velocity as a function energy and $\Sigma_i(\vec{r}, E)$ is the cross section for interaction type i in $d\vec{r}$ about \vec{r} and dE about E [16]. Energy dependent neutron flux, $v(E)N(\vec{r}, E)$, will not be known in an object *a priori*. Therefore only general statements about the presence of isotopes, not quantitative amounts, can be made from recorded gamma-ray spectra.

Gamma rays from inelastic scatter or neutron capture in region $d\vec{r}$ about \vec{r} can be localized spatially using gamma-ray imaging spectrometers. Typically only photopeak gamma rays are imaged. Cutting on photopeaks insures emitted gamma rays have traveled through

object shielding without subsequent interaction, which could change the apparent emission location, before detection. Assuming angularly isotropic detector efficiency, the number of detected, uninteracted, photopeak gamma rays per unit time from region $d\vec{r}$ about \vec{r} is

$$D_i(\vec{r}) = \frac{\Omega(\vec{r}) f_i \epsilon_i I_i(\vec{r})}{4\pi} \int_{\vec{R}_{\text{path}}} e^{-\Sigma_T(i, \vec{r}) d\vec{r}} \quad (2)$$

where ϵ_i is the detector photopeak efficiency at the photon energy emitted by reaction i , $\Sigma_T(i, \vec{r})$ is the macroscopic cross section at $d\vec{r}$ about \vec{r} at the photon energy emitted by reaction i , f_i is the fraction photon yield from interaction i , $\Omega(\vec{r})$ is the solid angle subtended by the detector for interactions at \vec{r} and \vec{R}_{path} is the path between \vec{r} and the detector.

Most single-view, gamma-ray imaging techniques cannot provide 3-D, spatial information on gamma rays emitted in the far field where there is no detector parallax. Due to this lack of parallax, gamma-ray

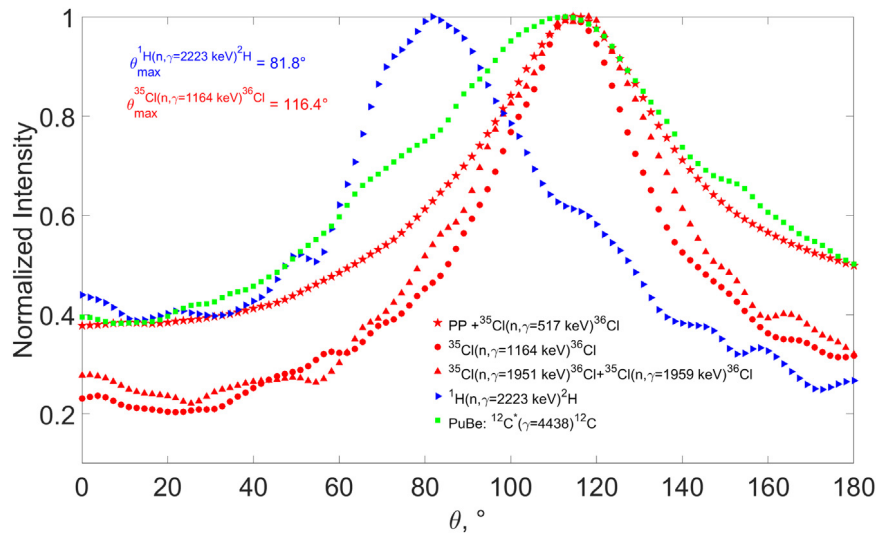


Fig. 6. Polar slices through each hotspot in Fig. 5. The separation between $^{35}\text{Cl}(n,\gamma)^{36}\text{Cl}$ hotspots, in red, and $^1\text{H}(n,\gamma)^2\text{H}$ hotspot in blue is roughly 35° . (For interpretation of the references to color in this figure legend, the reader is referred to the web version of this article.)

images are commonly reconstructed in a spherical, 2-D angular domain. In this imaging domain, the gamma-ray signal from spatial voxels in the same angular direction (θ, ϕ) are integrated together through

$$D_i(\theta, \phi) = \int_{\bar{R}(\theta, \phi)} D_i(\bar{r}) d\bar{r} \quad (3)$$

where $\bar{R}(\theta, \phi)$ is a ray in direction (θ, ϕ) starting from the detector. This undesirable integration prevents the estimation of voxelized intensities when using only a single measurement view. Therefore qualitative statements about isotopic distributions can only be made in the angular domain. However, research towards quantitative measurement of 3-D, elemental distributions is underway for small samples, placed in the near-field where there is large detector parallax, using a thermal neutron beam [17].

2.2. Detection and Compton imaging of high-energy gamma rays

Characteristic neutron induced gamma rays can be energetic, with energies exceeding several MeV, and detected using CdZnTe detectors and spatially localized via Compton imaging. In Compton imaging, gamma rays Compton scatter off detector electrons and are subsequently absorbed in another interaction. Incident gamma-ray direction can be localized to the surface of a cone by using Compton scatter kinematics and the lever arm between interactions [18].

High-energy gamma rays have a significant pair production cross section in CdZnTe. Pair production complicates Compton imaging as gamma rays that undergo pair production in their first interaction do not contain valid imaging information. Furthermore, these pair production events can occur in photopeaks if subsequent annihilation photons are absorbed. Therefore first-interaction, pair production events should be algorithmically excluded in high-energy Compton imaging measurements to maximize image quality. This is particularly important for non-sparse scenes that contain regions of substantially different neutron-induced gamma-ray production rates. Otherwise, systematic artifacts in the Compton image of a strong region of neutron-induced gamma rays may overwhelm, and obscure, a relatively weaker source region. Photopeak, pair production events can be naively discarded by removing events where any number of interaction energies sum to 511 keV within some error [19]. However for simplicity, this work does not attempt to remove any pair production events. These unwanted, pair production events were not expected to significantly degrade image quality in the sparse scene investigated. As such, all events within selected photopeaks were used in Compton reconstructions.

Large electron-hole clouds further complicate the imaging of high-energy gamma rays using CdZnTe detectors. The size of electron-hole clouds generated by high-energy gamma rays in CdZnTe is comparable to or larger than the dimension of pixelated electrodes used to collect signals [20]. When drifting through the detector, these large charge clouds have a large probability of being collected by more than one anode pixel, triggering them. Events with spatially contiguous clusters of triggered anode pixels require additional processing to estimate the true interaction locations [21]. Interaction location within each contiguous anode pixel cluster can be estimated using the energy-weighted mean of all triggered pixel locations, and subsequently used in calculating Compton imaging lever arms.

Photopeak Compton images also contain systematic artifacts from both incomplete energy deposition and object-scattered events. Incomplete energy deposition artifacts are particularly severe in scenarios with strong, high-energy gamma-ray emissions. For example, neutron capture on ^{35}Cl emits several strong gamma-ray lines above 6 MeV. Incomplete energy deposition events from bright, high-energy emissions can fall in lower energy photopeaks. These incomplete energy deposition events are erroneously selected, in addition to true photopeak events, when selecting specific isotopic emissions. Furthermore, the Compton scatter formula used to estimate Compton cone opening angle assume complete energy deposition. As such, Compton cones from these incomplete energy deposition events are systematically biased, producing artifacts [22]. Similarly, higher energy photons can self-scatter in the object of interest. These photons can downscatter into lower energy photopeak windows. Object-scattered photons are indistinguishable from true, uncollided photopeak photons. These object-scattered events are imaged as originating from the location of their last scatter, not emission, introducing an object-dependent image background. However, differential-imaging-based techniques can be used to mitigate the influence of both incomplete energy deposition and object-scattered events [23]. Compton images of incomplete energy deposition and object-scattered events are a weak function of recorded gamma-ray energy. As such, systematic artifacts in some photopeak Compton image can be estimated from a Compton reconstruction at slightly higher energy. The estimated artifact image, weighted by relative count rates, is then subtracted from the photopeak image containing a combination of true photopeak and erroneous events. This Compton-subtraction process, given sufficient measurement statistics, largely mitigates systematic artifacts from both incomplete energy deposition and object-scattered events. The differential imaging windows used in this work were immediately above in energy, and similar in width, to the photopeaks windows of interest.

Previous high-energy, gamma-ray measurements using CdZnTe crystals readout by analog application specific integrated circuits (ASICs) suffered from insufficient dynamic range, where many events with saturated signals were discarded [24]. The dynamic range of new digital ASICs has been increased to 7 MeV, mitigating the signal saturation problem of analog CdZnTe detectors [25]. Transient signals in large, anode pixel clusters also degraded the energy resolution of high-energy photopeaks in analog CdZnTe systems [26]. Using full waveforms from CdZnTe readout using digital ASICs, transient signal crosstalk can be corrected, improving the energy resolution of high-energy photopeaks [25]. Improved energy resolution enables imaging of specific isotopes by cutting on characteristic photopeaks from neutron induced gamma rays.

3. Detector system

Various detectors have been used to detect neutron-induced gamma rays. High-efficiency spectroscopic systems using either LaBr₃ and NaI(Tl) have demonstrated detection of both explosives and common cargo materials via active interrogation using a DT generator [27,28]. However, scintillator-based systems are plagued by intrinsically poor energy resolution. Without sufficient energy resolution it is difficult to cut on photopeaks which consist of uncollided flux. Limitations in accurate event position-sensing, which is needed for Compton imaging, also complicates the use of large, monolithic scintillators. As such, high energy resolution HPGe detectors are commonly used to detect neutron-induced gamma rays with high efficiency. For example, the PINS system from Idaho National Laboratory uses a large, 50% efficient HPGe detector to quantify neutron-induced gamma rays from artillery shells [29]. Some HPGe-based detectors also offer Compton imaging through the use of position-sensing cross-strip electrodes [14]. However, all HPGe-based systems are complicated by the logistical constraints inherent to cryogenic cooling. In contrast, advancements in digital CdZnTe systems have substantially narrowed the historic energy resolution gap between CdZnTe and HPGe detectors at room-temperature [30]. Furthermore, advances in crystal growth have pushed the boundaries of crystal size such that efficient, monolithic, 24 cm³ detectors are viable [31]. Future improvements in both CdZnTe energy resolution and efficiency are expected with new readout ASICs and crystal fabrication techniques. As such, this initial demonstration measurement was conducted with CdZnTe detectors in anticipation of future improvements in both energy resolution and efficiency.

A 3 by 3 array of 2 × 2 × 1.5 cm³ CdZnTe crystals was used to detect and Compton image gamma rays. Each crystal was instrumented with an 11 × 11 array of pixelated anodes and a planar cathode. The pixelated anode geometry provided the absolute (x,y) location of gamma-ray interactions while the cathode-to-anode ratio or drift time was used to estimate z [32]. Signals were digitized by VAD_UM2.2 digital ASICs [25]. Coincident interactions between individual crystals were detectable for an effective, total detector mass of roughly 300 g. Nominal energy resolution was 0.44, 0.46, and 0.65% full-width-at-half-maximum (FWHM) at 662 keV using 700, 3000 and 7000 keV dynamic ranges respectively for all-events. Detailed description of a similar digital CdZnTe systems are found in [33].

4. Experimental setup

Large polyvinyl chloride (PVC: C₂H₃Cl) and polyethylene (PE: C₂H₄) neutron targets were manufactured. The PVC target was constructed using six, 2.5 × 30 × 30 cm³ PVC sheets held together by PVC dowels. A 5 cm diameter hole was drilled in five of the six PVC layers to allow for neutron source insertion. The PE target was a right-circular cylinder of 30 cm radius and 12 cm height. The targets were combined, separated by a hollow PE spacer, forming a ‘dumbbell’ shape. A ²³⁸PuBe source was inserted into the PVC target hole. A technical drawing and photograph of the dumbbell geometry is shown in Fig. 1.

The CdZnTe detector was placed 45 cm away from the dumbbell centerline and elevated 10 cm above the table surface. Spectra and Compton images were collected over a three hour dwell at a 8.5 mR/h gamma-ray dose rate which corresponded to 2000 recorded counts per second. A low, 100 keV low-energy-threshold was chosen, although it induced substantial detector dead time, to insure low energy interactions in Compton scatter events were recorded.

5. Simulated results

The dumbbell geometry was simulated using MCNP-PoliMi with PVC and PE material compositions taken from the PNNL Material Compendium [34,35]. Neutron inelastic scatter and capture cross sections for elements in the plastic targets were plotted in Fig. 2 for clarity while gamma rays emitted from each element are tabulated in Table 1. Hydrogen, chlorine and carbon inelastic scatter and capture locations were extracted from the collision file and plotted in Fig. 3. ³⁵Cl has a much larger neutron capture cross section than ¹H, causing a great majority of PVC neutron captures to occur on ³⁵Cl. In PE, ¹H capture dominates over ¹²C capture. Adding the low-mass spacer produces strong, spatially separated regions of mostly ¹H and ³⁵Cl neutron capture. This spatial separation corresponds to an angular separation of about 33° at a standoff of 45 cm. This angular separation is well within the resolving power of CdZnTe Compton imaging systems.

6. Measured results

Spectra from a measurement of PVC alone and the combined PVC/PE dumbbell were plotted in Fig. 4. Focusing in on the 1800–2400 keV spectral region, we see ³⁵Cl and ¹H capture peaks at 1.9 and 2.2 MeV respectively. When the PE target is added, we see relatively more ¹H capture when compared to the PVC target alone. Clearly, the addition of PE introduced additional ¹H capture. Evidence of thermal neutron capture on ¹¹³Cd and ¹⁰B in the CdZnTe detector and printed circuit boards is seen with peaks at 558 and 478 keV respectively [36]. Furthermore, Doppler broadened 4.4 MeV gamma rays from the deexcitation of ¹²*C from ⁹Be(α,n)¹²*C in the PuBe source itself is seen.

Compton images were generated using simple back-projection binning on ³⁵Cl and ¹H capture gamma-ray energies and shown in Fig. 5. Compton images binning on 517, 1164 and 1951/1959 keV ³⁵Cl emissions show clear source hotspots around (θ, φ) = (116, 273)°. Notably, the 517 keV Compton image from ³⁵Cl capture is slightly contaminated by annihilation photons from pair production of higher energy gamma rays in the targets. It is hypothesized the bulk of these annihilation photons originate from interactions of 4.4 MeV PuBe gamma rays in the PVC target. Further binning on the 4.4 MeV ¹²*C deexcitation line produces a hotspot in a similar direction to ³⁵Cl gamma rays. This is unsurprising as the PuBe source was placed inside the PVC target. Contrastingly, binning on the 2234 keV emission of neutron capture on ¹H produces a hotspot at the different location of (θ, φ) = (82, 270)°. Polar slices through the center of Compton hotspots are shown in Fig. 6 emphasizing the similar locations of ³⁵Cl and ¹²*C hotspots which are well separated from ¹H. Taking the maximum of each polar slice as the hotspot centroid, ³⁵Cl and ¹H captures appear separated by roughly 34° in the polar dimension which agrees well with the value predicted from simulation. This shows that neutron induced gamma rays can be Compton imaged to provide angularly resolved estimates of shielding material isotopics.

7. Conclusion

A single plane of 3 × 3 CdZnTe detectors has successfully separated the spatial distribution of ¹H and ³⁵Cl captures in PE and PVC targets using Compton imaging. Compton images of ³⁵Cl(n,γ)³⁶Cl and ¹²*C(γ)¹²C gamma rays appear in a self-consistent location while the measured angular separation of 33° to the region of intense ¹H(n,γ)²H capture was

Table 1

Prominent capture and inelastic gamma rays produced by chlorine, hydrogen and carbon [13] with corresponding isotopic abundances [12].

Element, % abundance	Capture, E (keV)	Inelastic, E (keV)
³⁵ Cl, 75.8%	517.1, 786.3, 788.4 1164.9, 1170.9 1951.1, 1959.3, 2863.8, 6111.0 6619.7, 6627.9, 7414.1, 7790.5	1219.3, 1796.0, 2645.7 2693.8, 3002.3, 3162.8
¹ H, 99.99%	2223.3	N/A
¹² C, 98.9%	1100.0, 1261.8, 1270.0, 1860.0 3090.00, 3683.9, 4954.0, 4950.0	4438.9

consistent with MCNP-PoliMi simulation. This suggests that CdZnTe can be used to detect and spatially localize the presence of certain shielding isotopes in a neutron field. The isotope specific characterization of compound shields provides complimentary information to previous gamma-ray attenuation based techniques. Furthermore, the described technique can be implemented on current, fielded gamma-ray imaging systems without hardware modification.

Detection and imaging of high-energy, neutron induced gamma rays requires high efficiency detection systems. A more efficient CdZnTe system, consisting of four, 3 by 3 planes of $2.0 \times 2.0 \times 1.5$ cm³ crystals, is currently under development. With active mass exceeding 1 kg, the detection efficiency of high-energy gamma rays should be greatly improved. Image quality from the larger system will also improve as the average length of Compton cone lever arms increases with additional planes. This occurs as uncertainty in the opening angle of Compton cones is dominated by relative position uncertainty [37]: as lever arms between interactions become longer, the relative angular uncertainty from voxelized position uncertainty decreases.

Analysis can be extended to hypothetical cases of shielded SNM using a proposed, four-plane CdZnTe system. Notably, this proposed system corresponds to roughly a factor of four increase in efficiency, when tiling the planes side-by-side, compared to the detector used in this work. CdZnTe systems of similar size are commercially available for imaging the prompt gamma rays emitted during proton cancer therapy [38]. Furthermore, detector dead time can be substantially reduced at high count rates by increasing the system low-energy threshold. This would substantially improve the absolute system efficiency to high-energy, neutron-induced gamma rays from bright objects.

The low spontaneous fission rate of highly-enriched uranium precludes shielding analysis using neutrons from self-interrogation. In contrast, the spontaneous fission rate of weapons-grade plutonium is several orders of magnitude more intense than highly-enriched uranium, enabling self-interrogation-based shielding analysis [5]. The BERP ball, a 4.5 kg sphere of weapons-grade plutonium, is a well-known object that can serve as a hypothetical, plutonium-based nuclear weapon using the Fetter model [5,39]. The spontaneous fission rate of the bare BERP ball is around $3 \cdot 10^5$ n/s with a non-negligible leakage multiplication of about 3. When moderated by hydrogenous material, such as 3 inches of polyethylene, the leakage multiplication is increased to roughly 10 [40]. Assuming a leakage multiplication of 10, which is reasonable considering the 10 cm of hydrogenous high explosives used in the Fetter model, the expected, leaked neutron flux is roughly $3 \cdot 10^6$ n/s. The leaked neutron flux from the moderated BERP ball discussed above is about an order-of-magnitude less intense than the neutron source used in this work. However, gains in system efficiency, a factor of four from using multiple detector planes and conservatively a factor of two from decreased system dead time, make practical measurement of shielding isotopes around moderated, plutonium pits appear feasible on the scale of hours.

In measurements where long dwell times are untenable, active interrogation may be used to enhance signal strength. Subsequent measurements should be conducted with other compound shields, such as nitrogen-rich high-explosives like HMX (C₄H₈N₈O₈) [35]. Demonstrated techniques are directly applicable to other prompt gamma-ray neutron activation analysis measurements, such as the PINS system, developed for interrogating high explosive and chemical weapon artillery shells [29]. Compton imaging of neutron-induced gamma rays should also be tested on HPGe based Compton imaging spectrometers.

Acknowledgments

The authors would like to thank their current colleagues in the Orion Radiation Measurement Group and past group members whose work is leveraged here. This material is based upon work supported by the National Science Foundation Graduate Research Fellowship under Grant No. DGE 1256260. The digital, 3-D CdZnTe detector technology has been developed under funding support from the US Department of Defense, Defense Threat Reduction Agency under award #HDTRA1-15-C-0049. Any opinions, findings and conclusions or recommendations expressed in this material are those of the authors and do not necessarily reflect the views of the Defense Threat Reduction Agency.

References

- [1] R.J.S. Harry, J.K. Aaldijk, J.P. Braak, Gamma-Spectrometric Determination of Isotopic Composition Without Use of Standards, Tech. rep, IAEA, 1976.
- [2] T.E. Sampson, S. Hsue, J. Parker, S. Johnson, D.F. Bowersox, The determination of plutonium isotopic composition by Gamma-ray spectroscopy, Nucl. Instrum. Methods Phys. Res. A 193 (1982) 177–183.
- [3] R. Berndt, E. Franke, P. Mortreau, 235U enrichment or UF₆ mass determination on UF₆ cylinders with non-destructive analysis methods, Nucl. Instrum. Methods Phys. Res. A 612 (2) (2010) 309–319, <http://dx.doi.org/10.1016/j.nima.2009.10.060>, URL <http://dx.doi.org/10.1016/j.nima.2009.10.060>.
- [4] A framework document with terms and definitions, principles, and good practices: Principles for nuclear disarmament verification, Tech. rep., International Partnership for Nuclear Disarmament Verification, 2017, URL <http://ipndv.org/wp-content/uploads/2017/11/WG1-Deliverable-One-Final-.pdf>.
- [5] S. Fetter, V.A. Frolov, M. Miller, R. Mozley, O.F. Prilutsky, S.N. Rodionov, R.Z. Sagdeev, Detecting nuclear warheads, Sci. Glob. Secur. 1 (1990) 225–302.
- [6] R.C. Runkle, D.L. Chichester, S.J. Thompson, Rattling nucleons: New developments in active interrogation of special nuclear material, Nucl. Instrum. Methods A 663 (2012) 75–95, <http://dx.doi.org/10.1016/j.nima.2011.09.052>.
- [7] D.T. Reilly, N. Ensslin, H.J. Smith, S. Kreiner, Passive Nondestructive Assay of Nuclear Materials, Los Alamos National Laboratory, Washington, D.C., 1991.
- [8] S.M. Horne, G.G. Thoreson, L.A. Theisen, D.J. Mitchell, L. Harding, A. Wendy, Gadrar-drf 185 user's manual, Tech. rep., Sandia National Laboratories, Albuquerque, New Mexico, 2014.
- [9] M. Streicher, S. Brown, Y. Zhu, D. Goodman, Z. He, A method to estimate the atomic number and mass thickness of intervening materials in uranium and plutonium Gamma-ray spectroscopy measurements, IEEE Trans. Nucl. Sci. 63 (5) (2016) 2639–2648.
- [10] D. Goodman, S. Brown, J. Chu, Z. He, Angular detection and shielding characterization of simulated U-235 using time encoded imaging and 3D position sensitive CdZnTe detectors, in: IEEE Room Temperature Semiconductor Detectors Conference Record, 2017.
- [11] D. Goodman, M. Streicher, Y. Zhu, Z. He, Identification of intervening materials in Gamma-ray spectroscopy measurements using angularly deconvolved spectra with multiple sources in the field-of-view, IEEE Trans. Nucl. Sci. 65 (3) (2018).
- [12] J.S. Coursey, D.J. Schwab, J.J. Tsai, R.A. Dragoset, Atomic Weights and Isotopic Compositions (Version 4.1), National Institute of Standards and Technology, Gaithersburg, MD., 2015, URL https://physics.nist.gov/cgi-bin/Compositions/stand_alone.pl.
- [13] A.A. Sonzogni, NuDat 2.0: Nuclear structure and decay data on the internet, in: AIP Conference Proceedings, Vol. 769, 2005, pp. 574–577, <http://dx.doi.org/10.1063/1.1945075>.
- [14] PHDS Co., Germanium Gamma ray imaging detectors, 2017, URL <http://phdsc.com>.
- [15] C.G. Wahl, W.R. Kaye, W. Wang, F. Zhang, J.M. Jaworski, A. King, Y.A. Boucher, Z. He, The Polaris-H imaging spectrometer, Nucl. Instrum. Methods Phys. Res. A 784 (2015) 377–381.
- [16] J. Duderstadt, L. Hamilton, Nuclear Reactor Analysis, John Wiley & Sons, New York, New York, 1976.

- [17] H. Chen, H. Chen-Mayer, D. Turkoglu, R. Benjamin, E. Draeger, J. Polf, Spectroscopic Compton imaging of prompt Gamma emissions at the MeV energy range, *J. Radioanal. Nucl. Chem.* 318 (1) (2018) 241–246.
- [18] R.W. Todd, J.M. Nightingale, D.B. Everett, A proposed γ camera, *Nature* 251 (5471) (1974) 132–134, <http://dx.doi.org/10.1038/251132a0>.
- [19] S.E. Boggs, P. Jean, Event reconstruction in high resolution Compton telescopes, *Astron. Astrophys. Suppl. Ser.* 145 (2000) 311–321.
- [20] Y. Zhu, Digital Signal Processing Methods for Pixelated 3-D Position Sensitive Room-Temperature Semiconductor Detectors (Ph.D. thesis), University of Michigan, 2012.
- [21] W. Wang, W.R. Kaye, J.C. Kim, F. Zhang, Z. He, Improvement of Compton imaging efficiency by using side-neighbor events, *Nucl. Instrum. Methods A* 687 (2012) 62–68.
- [22] J. Chu, Advanced Imaging Algorithms with Position-Sensitive Gamma-Ray Detectors, (Ph.D. thesis), University of Michigan, 2018.
- [23] H. Zhong, W. Wang, W. Kaye, C. Wahl, J. Jaworski, Reduction of background interference in a radiation image, 2018.
- [24] Y.A. Boucher, F. Zhang, W. Kaye, Z. He, Measurements of Gamma Rays above 3 MeV using 3D Position-Sensitive $20 \times 20 \times 15$ mm CdZnTe Detectors, in: IEEE Nuclear Science Symposium, 2011, pp. 4540–4544.
- [25] M.W. Streicher, Applications of Digitized 3-D Position-Sensitive CdZnTe Spectrometers for National Security and Nuclear Nonproliferation (Ph.D. thesis), University of Michigan, 2017.
- [26] Y.A. Boucher, Analysis of Cadmium Zinc Telluride Detector Performance and Characteristics for Applications in Gamma-Ray Imaging Spectrometers (Ph.D. thesis), University of Michigan, 2013.
- [27] C. Eleon, B. Perot, C. Carasco, D. Sudac, J. Obhodas, V. Valkovic, M. Carlo, Experimental and MCNP simulated Gamma-ray spectra for the UNCOSS neutron-based explosive detector, *Nucl. Instrum. Methods Phys. Res. A* 629 (2011) 220–229, <http://dx.doi.org/10.1016/j.nima.2010.11.055>, URL <http://dx.doi.org/10.1016/j.nima.2010.11.055>.
- [28] B. Perot, C. Carasco, S. Bernard, A. Mariani, J. Szabo, G. Sannie, V. Valkovic, D. Sudac, G. Viesti, M. Lunardon, C. Botosso, G. Nebbia, S. Pesente, S. Moretto, A. Zenoni, A. Donzella, M. Mosynski, M. Gierlik, W. Klamra, P. Tourneur, M. Lhuissier, A. Colonna, C. Tintori, P. Peerani, V. Sequeria, M. Salvato, Measurement of 14 MeV neutron-induced prompt gamma-ray spectra from 15 elements found in cargo containers, *Appl. Radiat. Isot.* 66 (2008) 421–434, <http://dx.doi.org/10.1016/j.apradiso.2007.11.011>.
- [29] A.J. Caffrey, J.D. Cole, R.J. Gehrke, R.C. Greenwood, Chemical warfare agent and high explosive identification by spectroscopy of neutron-induced gamma rays, *IEEE Trans. Nucl. Sci.* 39 (5) (1992) 1422–1426, <http://dx.doi.org/10.1109/23.173218>.
- [30] Y. Zhu, M. Streicher, J. Xia, Z. He, Energy resolution improvement and high-energy photon detection in CdZnTe spectrometers with second generation digital electronics and reduced preamplifier trace length, 2018, submitted for publication.
- [31] H. Chen, H. Li, M. Reed, A. Sundaram, J. Eger, J. Hugg, S. Abbaszadeh, M. Li, G. Montemont, L. Verger, Y. Zhu, Z. He, Development of large-volume high-performance monolithic CZT radiation detector, in: SPIE Proceedings on Hard X-Ray, Gamma-Ray, and Neutron Detector Physics XX, 2019, <http://dx.doi.org/10.1117/12.2321244>.
- [32] Z. He, G.F. Knoll, D.K. Wehe, R. Rojeski, C.H. Mastraneg, 1-D position sensitive single carrier semiconductor detectors, *Nucl. Instrum. Methods Phys. Res. A* 380 (1996) 228–231.
- [33] M. Streicher, Y. Zhu, F. Zhang, Y.A. Boucher, C.G. Wahl, H. Yang, Z. He, A portable 2×2 digital 3D CZT imaging spectrometer system, in: IEEE Nuclear Science Symposium and Medical Imaging Conference, 2014.
- [34] S.A. Pozzi, E. Padovani, M. Marseguerra, MCNP-PoliMi: a Monte-Carlo code for correlation measurements, *Nucl. Instrum. Methods Phys. Res. A* 513 (2003) 550–558, <http://dx.doi.org/10.1016/j.nima.2003.06.012>.
- [35] R.J. McConn, C.J. Gesh, R.T. Pagh, R.A. Rucker, R.G. Williams, Compendium of material composition data for radiation transport modeling, Tech. rep., Pacific Northwest National Laboratory, 2011.
- [36] S. Brown, Time-Encoded Thermal Neutron Imaging Using Large-Volume Pixelated CdZnTe Detectors (Ph.D. thesis), University of Michigan, 2017.
- [37] D. Xu, Gamma-Ray Imaging and Polarization Measurement Using 3-D Position-Sensitive CdZnTe Detectors (Ph.D. thesis), University of Michigan, 2006.
- [38] J.C. Polf, S. Avery, D.S. Mackin, S. Beddar, Imaging of prompt gamma rays emitted during delivery of clinical proton beams with a Compton camera: feasibility studies for range verification, *Phys. Med. Biol.* 60 (18) (2015) 7085–7099, <http://dx.doi.org/10.1088/0031-9155/60/18/7085>.
- [39] J. Hutchinson, W. Myers, R. Sanchez, D. Hayes, Analysis of the Berp ball: an alpha-phase plutonium sphere, Tech. rep., Los Alamos National Laboratory, 2009.
- [40] J. Hutchinson, C. Solomon, A. Sood, W. Myers, M. Smith-Nelson, Comparison of Feynman Variance-to-Mean Measurements Using Measured and Simulated Data, in: International Conference on Nuclear Criticality, 2011.